A&A 669, A134 (2023)
https://doi.org/10.1051/0004-6361/202243855

Astronomy & Astrophysics

A powerful (and likely young) radio-loud quasar at $z = 5.3$

S. Belladitta[1,2], A. Moretti[1], A. Caccianiga[1], D. Dallacasa[3,4], C. Spingola[4], M. Pedani[5], L. P. Cassarà[6], and S. Bisogni[6]

[1] INAF – Osservatorio Astronomico di Brera, Via Brera, 28, 20121 Milano, Italy
e-mail: silvia.belladitta@inaf.it
[2] DiSAT, Università degli Studi dell'Insubria, Via Valleggio 11, 22100 Como, Italy
[3] Dipartimento di Fisica e Astronomia, Università degli Studi di Bologna, Via Gobetti 93/2, 40129 Bologna, Italy
[4] INAF – Istituto di Radioastronomia, Via Gobetti 101, 40129 Bologna, Italy
[5] INAF – Fundación Galileo Galilei, Rambla José Ana Fernandez Pérez 7, 38712 Breña Baja, TF, Spain
[6] INAF – Istituto di Astrofisica Spaziale e Fisica Cosmica (IASF), Via A. Corti 12, 20133 Milano, Italy

Received 24 April 2022 / Accepted 20 October 2022

ABSTRACT

We present the discovery of PSO J191.05696+86.43172 (hereafter PSO J191+86), a new powerful radio-loud quasar (QSO) in the early Universe ($z = 5.32$). We discovered it by cross-matching the NRAO VLA Sky Survey (NVSS) radio catalog at 1.4 GHz with the first data release of the Panoramic Survey Telescope and Rapid Response System (Pan-STARRS PS1) in the optical. With a NVSS flux density of 74.2 mJy, PSO J191+86 is one of the brightest radio QSO discovered at $z \sim 5$. The intensity of its radio emission is also confirmed by the very high value of radio loudness ($R > 300$). The observed radio spectrum of PSO J191+86 shows a possible turnover around ∼1 GHz (i.e., ∼6 GHz in the rest frame), making it a gigahertz-peaked spectrum (GPS) source. However, variability could affect the real shape of the radio spectrum, because the data in hand were taken ∼25 years apart. By assuming a peak in the observed radio spectrum between 1 and 2 GHz (i.e., ∼6 and 13 GHz in the rest-frame) we find a linear size of the source of ∼10–30 pc and a corresponding kinetic age of 150–460 yr. This would make PSO J191+86 a newly born radio source. However, the large X-ray luminosity ($5.3{\times}10^{45}$ erg s^{-1}), the flat X-ray photon index ($\Gamma_X = 1.32$), and the optical–X-ray spectral index ($\tilde{\alpha_{ox}} = 1.329$) are typical of blazars. This could indicate that the nonthermal emission of PSO J191+86 is Doppler boosted. Further radio observations (both on arcsec and parsec scales) are necessary to better investigate the nature of this powerful radio QSO.

Key words. galaxies: active – galaxies: high-redshift – galaxies: jets – quasars: supermassive black holes – quasars: individual: PSO J191.05696+86.43172

1. Introduction

Radio-loud (RL) active galactic nuclei (AGN) are those supermassive black holes (SMBHs) that are able to expel part of the accreting matter into two relativistic bipolar jets (e.g., see Blandford et al. 2019 for a recent review). They are therefore usually referred to as jetted AGN (e.g., Padovani et al. 2017) and represent up to 10% of the total AGN population (e.g., Liu et al. 2021). Understanding the mechanisms responsible for the launch and the emission of these jets is of crucial importance for studying their role in SMBH accretion and evolution (e.g., Volonteri et al. 2015), and for investigating their feedback on the intergalactic medium (e.g., Fabian 2012).

High-redshift RL quasars (QSOs) are indispensable tools for studying the early evolutionary stage of the first jetted SMBHs, their feedback on the host galaxy and the environment, and their contribution to the re-ionization epoch (e.g., Blandford et al. 2019). Among the more than 500 QSOs discovered to date at $z > 5$, approximately 30 are classified as RL (e.g., Romani et al. 2004; McGreer et al. 2006; Zeimann et al. 2011; Sbarrato et al. 2012; Bañados et al. 2018), that is, with a radio loudness $R > 10$, with R defined as the ratio of the 5 GHz and 4400 Å rest-frame flux densities: $R = S_{5\,\mathrm{GHz}}/S_{4400\,\text{Å}}$ (Kellermann et al. 1989). Therefore, a systematic search for these objects and their subsequent study is necessary to better constrain the properties of jetted SMBHs in the first gigayears following the Big Bang.

In an effort to enlarge the current sample of high-z RL QSOs, we are conducting a project that combines optical, infrared (IR), and radio datasets to identify distant radio sources all over the sky (Caccianiga et al. 2019; Belladitta et al. 2019, 2020; Ighina et al. 2023). In this paper, we present the discovery and first observations of PSO J191.05696+86.43172 (hereafter PSO J191+86), a powerful jetted QSO at $z = 5.32$, which was selected from the cross-correlation of the NRAO VLA Sky Survey (NVSS, Condon et al. 1998) in the radio, the Panoramic Survey Telescope and Rapid Response System (Pan-STARRS PS1, Chambers et al. 2016) in the optical, and the AllWISE Source Catalog (Wright et al. 2010; Mainzer et al. 2011) in the mid-infrared (MIR).

The paper is organized as follows: in Sect. 2 we outline our selection method; in Sect. 3 we present new optical and near-infrared (NIR) spectroscopic observations of PSO J191+86; in Sects. 4 and 5 we report archival radio data and a new X-ray follow-up observation, respectively; in Sects. 6 and 7 we describe our results on the multi-wavelength properties of the source; and finally, in Sect. 8 we provide a brief discussion and conclusions.

The magnitudes used in this work are all in the AB system unless otherwise specified. We use a flat Λ cold dark matter (ΛCDM) cosmology with $H_0 = 70\,\mathrm{km\,s^{-1}\,Mpc^{-1}}$, $\Omega_m = 0.3$, and $\Omega_\Lambda = 0.7$. Spectral indices are given assuming $S_\nu \propto \nu^{-\alpha}$ and all errors are reported at 1σ, unless otherwise specified. Throughout

Table 1. Optical and MIR magnitudes of PSO J191+86.

Filter	Central λ (μm)	Mag (AB)	Ref. survey
(1)	(2)	(3)	(4)
r_{PS1}	0.680	21.34 ± 0.15	PS1
i_{PS1}	0.745	19.78 ± 0.04	PS1
z_{PS1}	0.870	19.49 ± 0.03	PS1
y_{PS1}	0.978	19.22 ± 0.06	PS1
$W1$	3.4	18.502 ± 0.035	WISE
$W2$	4.6	18.386 ± 0.051	WISE

Notes. Column (1): optical and MIR filters; Col. (2): filter central wavelength in μm; Col. (3): observed AB de-reddened magnitude; Col. (4): reference catalog. The offset between the Pan-STARRS PS1 optical and WISE MIR positions is 0.85″. The relations to convert from Vega to AB systems are: $W1_{AB} = W1 + 2.683$; $W2_{AB} = W2 + 3.319$ (Cutri et al. 2012).

the paper, the flux densities are the observed ones, while luminosities are given in the rest-frame of the source unless otherwise specified.

2. Source selection

From the entire NVSS catalog, we selected bright ($S_{1.4GHz} \geq 30$ mJy) and compact objects to provide an accurate (<2″) radio position. With this criteria we found approximately 45 000 sources. We then cross-matched these with the Pan-STARRS PS1 catalog using a maximum separation equal to 2″. This impact parameter guarantees the recovery of more than 90% of the real optical counterparts (Condon et al. 1998). We selected only relatively bright optical sources ($i_{PS1} < 21.5$) outside the Galactic plane ($|b| \geq 20°$) in order to minimize contamination from stars, and at Dec > −25° to exclude optical objects at the declination limit of the Pan-STARRS survey. All the sources that satisfied the following photometric criteria were then selected: (i) no detection in g_{PS1}-band; (ii) drop-out: $r_{PS1} - i_{PS1} \geq 1.2$; (iii) blue continuum: $i_{PS1} - z_{PS1} \leq 0.5$; (iv) point-like sources: $i_{PS1} - i_{Kron} < 0.05$; and (v) no detection in WISE (W2) or $i_{PS1} -$ W2(Vega) < 5. This last constraint has been placed to minimize the contamination by dust-reddened AGN at $z = 1 - 2$ (e.g., Carnall et al. 2015; Caccianiga et al. 2019).

Following the application of these filters, 14 candidates remained; 4 of them are known radio QSOs in the literature. PSO J191+86 stands out among the other 10 targets for its very high drop-out value ($r - i > 1.7$), its photometric redshift ($z > 5$), and its very high radio flux density ($S_{1.4\,GHz} > 70$ mJy). We therefore considered only this source for spectroscopic follow up. Table 1 reports the Pan-STARRS PS1 and WISE magnitudes of PSO J191+86 (corrected for Galactic extinction using the extinction law provided by Fitzpatrick (1999), with $R_V = 3.1$). Figure 1 shows the optical images of the source in the different g, r, i, z, y PS1 bands. The optical coordinates of PSO J191+86 are: RA = 191.05696 deg ($12^h44^m13.902^s$), Dec = +86.43172 deg ($+86^d25'54.07''$).

3. Optical and NIR observations, and data reduction

3.1. TNG/DOLORES observation

We performed a dedicated spectroscopic follow-up of PSO J191+86 with DOLORES (Device Optimized for the LOw RESolution) installed at the Telescopio Nazionale *Galileo* (TNG). We confirmed PSO J191+86 as a high-z RL QSO on the night of 21 June 2018, with a single 30min observation with the *LR–R* grism and a long-slit of 1″ width. The mean air mass during the observation was 1.7. Table 2 reports the details of this observation.

An exposure of an Ar+Ne+Hg+Kr lamp was carried out to ensure the wavelength calibration, and the flux calibration was obtained by observing the G191-B2B (RA = $05^h05^m30.62^s$, Dec = $+52^d49'54.0''$) spectro-photometric standard star of the catalogs of Oke (1990).

Data reduction was performed using standard Image Reduction and Analysis Facility (IRAF) procedures (Tody 1993). The DOLORES discovery spectrum is shown in Fig. 2; it has been corrected for Galactic extinction as explained in Sect. 2.

3.2. LBT/LUCI follow-up

We performed a spectroscopic follow-up with the Large Binocular Telescope (LBT) utility camera in the infrared (LUCI, Seifert et al. 2003) at the LBT in order to extend the wavelength range in the NIR band and detect the CIVλ1549 (hereafter CIV) and the MgIIλ2798 (hereafter MgII) broad emission lines (BELs), which can be used to estimate the central black hole mass of PSO J191+86 thanks to the so-called single epoch (SE) or virial method (e.g., Vestergaard & Peterson 2006, hereafter VP06, see Sect. 6.1). The observation was carried out on the night of 3 May 2019 (P.I. Moretti A., program ID: LBT2018AC123500-1) and consisted of 12 exposures of 270 s each in nodding mode in the sequence ABBA, with a total integration time of 1.8 h. The medium seeing along the night was 0.9″ and the mean air mass was 1.7. The details of this observation are reported in Table 2. We decided to use the grism 200 with the zJ and HK filters on LUCI1 and LUCI2, respectively, in order to cover the whole spectral range and detect the CIV (LUCI1) and the MgII (LUCI2) simultaneously. The G200-zJ configuration allowed us to observe the wavelength range from 0.9 to 1.2 μm, where the CIV line is expected ($\lambda_{obs} = 9805$ Å at $z = 5.3$); instead the G200-HK configuration covers the range from 1.5 to 2.4 μm in which the MgII line falls (expected $\lambda_{obs} = 17\,700$ Å). Data reduction was performed at the Italian LBT Spectroscopic Reduction Center with the software developed for LBT spectroscopic data reduction (Gargiulo et al. 2022). Each spectral image was independently dark subtracted and flat-field corrected. Sky subtraction was done on 2D extracted, wavelength-calibrated spectra. Wavelength calibration was obtained by using several sky lines, reaching an rms of 0.25 Å on LUCI1 and 0.5 Å on LUCI2.

Figure 2 shows the LBT/LUCI1 and the LBT/LUCI2 spectra in which the CIV and the MgII BELs are detected, together with the CIII]λ1909+AlIIIλ1860+SiIII]λ1892 complex. Also, in this case, the two spectra have been corrected for Galactic extinction as in the TNG/DOLORES spectrum. We note that the MgII line suffers from the presence of an absorption feature (a residual of background subtraction; see gray line in Fig. 2 and the zoom in Fig. 6). When masking the absorption feature, the wide range of absorption results in a gap close to the line center.

4. Archival continuum radio data

In addition to the NVSS observation at 1.4 GHz ($S_{1.4\,GHz} = 74.2 \pm 2.3$ mJy, see also Fig. 3), PSO J191+86

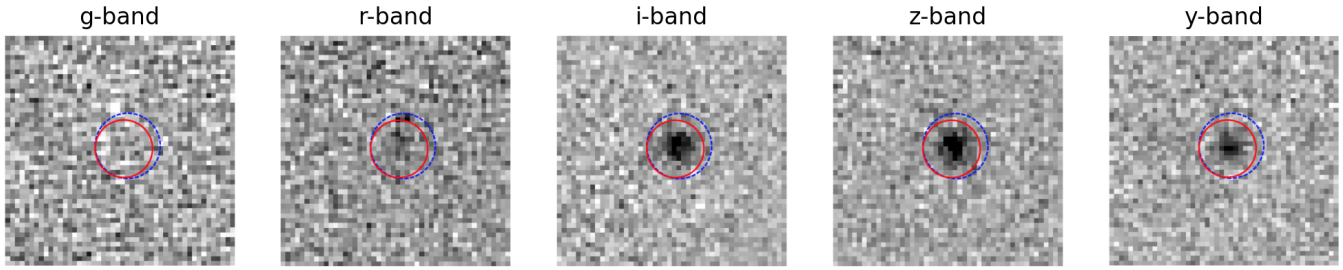

Fig. 1. $0.2' \times 0.2'$ Pan-STARRS PS1 g, r, i, z, y cutout images of PSO J191+86. Its optical position is marked with a red circle of $1.5''$ of diameter. The radio NVSS position is marked with a blue dashed circle, as large as the radio positional error reported in the catalog ($1.7''$). All images are oriented with north up and east to the left.

Table 2. Summary of the optical and NIR follow-up spectroscopic observations of PSO J191+86.

Date (1)	Telescope/instrument (2)	Exposure time (3)	*S/N* (4)
2018 June 21	TNG/DOLORES	0.5 h	∼7
2019 May 3	LBT/LUCI1	1.8 h	∼7.5
2019 May 3	LBT/LUCI2	1.8 h	∼7.5

Notes. Column (1): date of observation; Col. (2): telescope and instrument used; Col. (3): total exposure time; Col. (4): S/N of the continuum.

has an archival detection in the Westerbork Northern Sky Survey (WENSS, Rengelink et al. 1997, see Fig. 3) at 325 MHz of 19.0±3.3 mJy. Due to the availability of these two flux densities, Massaro et al. (2014) included PSO J191+86 in the LOw frequency Radio CATalog of flat spectrum sources (LORCAT). Moreover the source was observed by Healey et al. (2009) at 4.85 GHz with the Effelsberg 100 m telescope. These authors measured a flux density of 33.7±1.3 mJy. The detections with WENSS, NVSS, and Effelsberg enabled Healey et al. (2009) to classify PSO J191+86 as a Gigahertz-Peaked Spectrum (GPS) source, meaning a young ($<10^{3-4}$ yr) and compact (<1 kpc) radio source. These objects are usually considered to be the early stages of evolution of powerful large-scale radio galaxies of the local Universe (see O'Dea & Saikia 2021 for a recent review).

PSO J191+86 is also clearly detected at 3 GHz in the Very Large Array Sky Survey (VLASS, Lacy et al. 2020, see Figs. 3 and 4). The source was observed during both the first campaign of the first epoch (VLASS 1.1) in 2017 and the first campaign of the second epoch (VLASS 2.1) in 2020. As the data of the 1.1 epoch suffer from phase errors, that is, artifacts that alter the true size and morphology of a source, we carried out the analysis on only the 2.1 image. We performed a single Gaussian fit using the task IMFIT of the Common Astronomy Software Applications package (CASA, McMullin et al. 2007) to quantify the flux density and the size of PSO J191+86 (see Fig. 4). The measurements of total and peak flux density and the size obtained from the best fit are listed in Table 3. The position of the source estimated by the fit is: RA = $12^{h}44^{m}13.57949^{s} \pm 0.01239^{s}$, Dec = $+86^{d}25'54.04861'' \pm 0.00021^{s}$, which is at $0.3''$ from the optical PS1 position, confirming the radio–optical association of PSO J191+86. By comparing the dimensions of the source – as estimated by the single Gaussian fit – with the beam size (major axis = $4.372''$, minor axis = $2.241''$, PA = 80.75 deg, east of north), we concluded that the source is partially resolved.

Finally, PSO J191+86 is not detected in the TIFR GMRT Sky Survey (TGSS, Intema et al. 2017) at 150 MHz. From the TGSS image, we computed only an upper limit (at 2σ) of ∼4 mJy.

In Table 4, all the available radio flux densities of PSO J191+86 are reported. The VLASS integrated flux density has been corrected for 3% systematic uncertainty[1].

5. *Swift*-XRT follow up

PSO J191+86 was observed in X-rays by the *Swift*-XRT telescope (target ID: 3110833; P.I. Belladitta S.). Observations were carried out between September, October, and November 2020 and consisted of 44 segments for a total exposure time of 47.81 ks. Data have been reduced through the standard data-analysis pipeline (Evans et al. 2009), running on the UK *Swift* Science Data Centre web page[2] using HEASOFT v6.26.1. The source is clearly detected with a total of 55 counts and with an expected background of 7 counts in the [0.5–10] keV energy band. The standard (PSF-fitted) *Swift*-XRT position of the source calculated by the detected and centroid algorithm is RA = $12^{h}44^{m}12.97^{s}$, Dec = $+86^{d}25'57''$, with an uncertainty of $3.5''$ (90% confidence). This is at $3.0''$ from the optical PS1 position. A standard spectral analysis was performed using XSPEC (v.12.10.1) by fitting the observed spectrum (Fig. 5) with a single power law with the absorption factor fixed to the Galactic value (6.46×10^{20} cm^{-2}) as measured by the HI Galaxy map of Kalberla et al. (2005). We measured a photon index (Γ_X) of 1.32 ± 0.2, which implies an X-ray spectral index ($\alpha_X = \Gamma_X - 1$) of 0.32, and a flux of $8.11^{+1.63}_{-1.47} \times 10^{-14}$ erg s^{-1} cm^{-2} in the observed [0.5–10] keV energy band.

6. Analysis of MgII and CIV broad emission lines

Among all the emission lines detected in the TNG and LBT spectra, we focused on the CIV and MgII BELs; the latter allowed us to measure the redshift of the source and together with the CIV provides an estimation of the mass of the black hole hosted by PSO J191+86. To derive the properties of the two BELs (e.g., redshift, line width, line luminosity) we followed an approach used in several studies in the literature that is based on the analysis of high-z QSO spectra (e.g., Mazzucchelli et al. 2017; Schindler et al. 2020; Bañados et al. 2021; Vito et al. 2022; Farina et al. 2022).

First, we subtracted the continuum emission – which is described by a power law ($f_{pl} \propto \lambda/2500$ Å$^{\alpha_\lambda}$), an iron pseudo-continuum template, and a Balmer pseudo-continuum – from

[1] https://science.nrao.edu/vlass/data-access/vlass-epoch-1-quick-look-users-guide
[2] https://www.swift.ac.uk/index.php

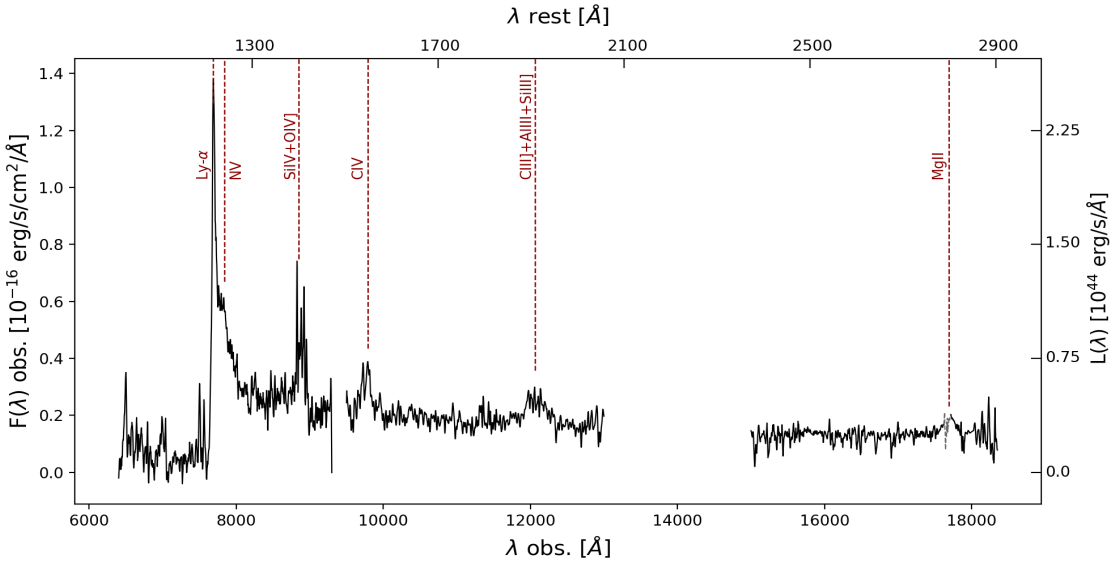

Fig. 2. Optical and NIR de-reddened observed spectra of PSO J191+86 taken at TNG and LBT, respectively. The most important visible emission lines are marked. We masked the part of the MgII line that suffers from a strong absorption feature, in which the peak of the MgII line falls (shown here in gray). The top x-axis reports the rest-frame wavelengths while the right axis shows the monochromatic luminosity.

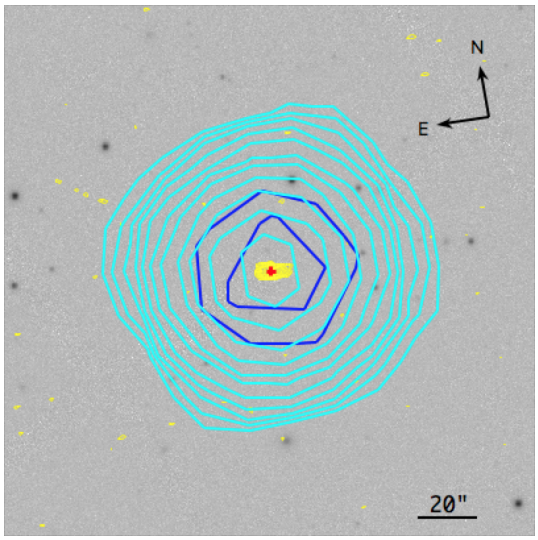

Fig. 3. 3′×3′ cutout of the $i_{\rm PS1}$ image around PSO J191+86 overlaid with the radio contours from NVSS (1.4 GHz, cyan), WENSS (325 MHz, blue), and VLASS (3 GHz, yellow). In all cases, contours are spaced by $\sqrt{2}$ starting from three times the survey rms (NVSS = 0.42 mJy beam^{-1}; VLASS = 160 μJy beam^{-1}; WENSS = 2.7 mJy beam^{-1}). A zoom onto the VLASS emission is shown in Fig. 4. The red cross indicates the optical position of the source.

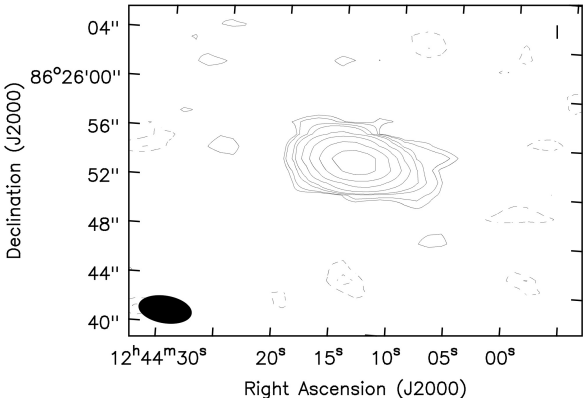

Fig. 4. VLASS 2.1 image of PSO J191+86. The contours are drawn at −3, −2, 2, 3, 6, 9, 18, 36, 72, and 144 times the off-source rms (160 μJy). In the bottom left corner, the beam size (4.372″ × 2.241″) is shown. North is up, east is left.

the spectra. We modeled the Fe II contribution with the empirical template of Vestergaard & Wilkes (2001), which is used in the derivation of the scaling relation that we later consider for estimating the black hole mass of the QSO (see Sect. 6.1). To be consistent with studies in the literature (e.g., Vito et al. 2022 and reference therein), we used an iterative process to convolve the iron pseudo-continuum model with a Gaussian function of equal width to that of the MgII emission line, as it is assumed that FeII emission arises from a region close to that responsible for the MgII emission. To perform the continuum fit, we chose a region of the quasar continuum free of broad emission lines and of strong spikes from residual atmospheric emission: [10 520–11 110] Å in the LUCI1 spectrum and [15 979–17 200] Å in the LUCI2 spectrum (see Fig. 6). We then subtracted the entire pseudo-continuum model from the observed spectra, and modeled the two BELs with Gaussian functions.

BELs are usually well described by a multiple-Gaussian profile (e.g., Marziani et al. 2010; Shen et al. 2011, 2019; Tang et al. 2012; Karouzos et al. 2015; Rakshit et al. 2020). In particular, we considered a model where each line is described by a broad plus a narrow component to account for a possible contribution from the narrow line region. Each broad line is modeled with 1 or 2 Gaussians, while the narrow component is modeled with a Gaussian that has a FWHM of lower than 1000 km s^{-1} and higher than the spectral resolution (FWHM $>\sim$ 200 km s^{-1}). In the case of MgII, we also considered that the line is a doublet (λ2796/2803) with an intensity ratio set equal to 1:1 (e.g., Marziani et al. 2013). For the MgII, we found that the narrow component is not statistically required and has no impact on the width of the broad component. The broad component of each line of the doublet is modeled with two Gaussian functions

Table 3. Properties of the quick-look VLASS 2.1 image of PSO J191+86.

Obs. (Rest) Freq. (GHz) (1)	Total flux density (mJy) (2)	Peak surface brightness (mJy beam^{-1}) (3)	Major axis (arcsec) (4)	Minor axis (arcsec) (5)	PA (deg) (6)
3.0 (18.96)	40.57±0.32	38.83±0.17	1.16±0.10	<0.39	75±7

Notes. Column (1): observing frequency (rest-frame frequency in parenthesis); Col. (2): integrated flux density; Col. (3): peak surface brightness; Cols. (4) and (5): de-convolved major and minor axes of the source estimated directly from the Gaussian fit; Col. (6) position angle (east of north).

Table 4. Summary of the archival radio observations of PSO J191+86.

Obs. freq. (GHz) (1)	S_ν (mJy) (2)	Survey or follow-up (3)	Resolution (arcsec) (4)	Obs. date (5)
0.150	$<\sim 4^a$	TGSS	25	15/03/2016
0.325	19.0±3.3	WENSS	15	15/06/1997
1.4	74.2±2.3	NVSS	45	24/06/1996
3.0	41.82±0.32	VLASS	2.5	30/08/2020
4.85	33.7±1.3	Effelsberg	150	June 2008

Notes. Column (1): observed frequency in GHz; Col. (2): integrated flux density in mJy; *a*: the TGSS value is an upper limit (at 2σ); Col. (3): reference survey or dedicated follow-up; Effelsberg refers to the observation carried out by Healey et al. (2009) with the 100 m Effelsberg telescope; Col. (4): angular resolution in arcsec; Col. (5): date of the observation.

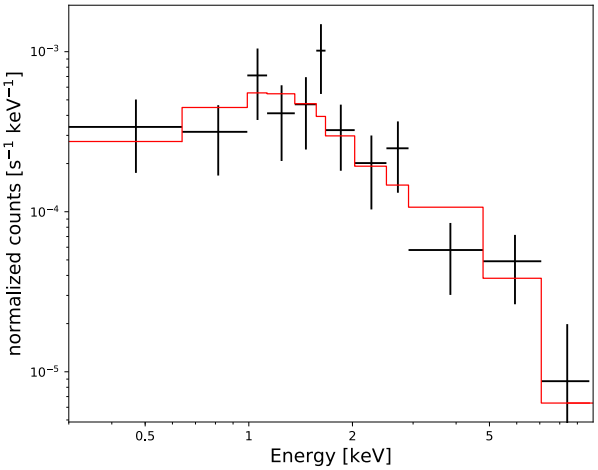

Fig. 5. *Swift*-XRT observed spectrum of PSO J191+86 modeled with a single power law with only Galactic absorption (solid red line).

(i.e., four Gaussians in total for describing the entire line profile; see Fig. 6). Similarly, for the CIV we did not find clear evidence of a narrow component. This is in agreement with several works in the literature, which report that the existence of a strong narrow component for the CIV line is controversial (e.g., Wills et al. 1993; Corbin & Boroson 1996; Vestergaard 2002; Shen & Liu 2012). Instead, the broad component is well fitted with a single Gaussian (Fig. 6). On the right side of the CIV, we also fitted with a single Gaussian profile the Heλ1640 emission line (see Fig. 6).

The uncertainties on broad emission line properties were evaluated through a Monte Carlo method (e.g., Raiteri et al. 2020; Zuo et al. 2020; Diana et al. 2022). Each wavelength of the best-fit model was randomly perturbed 1000 times according to a Gaussian distribution of the mean rms of the spectra computed underneath the emission lines on the pseudo-continuum-subtracted spectrum. In this way, we obtained 1000 different mock spectra of the line profiles, from which we measured the line properties with the same procedure as that used on the real data. We computed the distributions of all the line properties for these 1000 simulated spectra, and the interval that contains 68% of the data in these distributions was taken as the statistical uncertainty on the best-fit values.

From the multi-Gaussian modeling, we measured the following line parameters: redshift, line width (parameterized as the FWHM), rest-frame equivalent width (REW), line flux, and luminosity (see Table 5). As the systemic redshift of PSO J191+86, we adopted the one derived from the MgII line, which is usually taken as the best redshift estimator for high-z objects when submillimeter and millimeter data are not available (e.g., De Rosa et al. 2014; Mazzucchelli et al. 2017; Schindler et al. 2020). We note that, despite the absorption feature in the middle, the redshift estimated from the MgII line is consistent with the expected positions of the Ly$_\alpha$ and NV lines (see right panel of Fig. 6).

6.1. Estimates of the black hole mass

The most common method used to compute the mass of the central BH of Type I AGN is the SE method (e.g., Mazzucchelli et al. 2017; Shen et al. 2011, 2019; Diana et al. 2022). The underlying assumption of this technique is that the dynamics of the gas clouds is dominated by the central black hole gravitational potential. CIV and MgII BELs are the lines most frequently used to compute the mass of the central SMBH hosted by high-z QSOs. However, several works have questioned the reliability of CIV as a good virial mass indicator (e.g., Sulentic et al. 2007; Trakhtenbrot & Netzer 2012; Bisogni et al. 2017; Marziani et al. 2019) due to its observed blueward asymmetry and the velocity shifts of the line profile with respect to low-ionization lines, which are independent of the source orientation (e.g., Gaskell 1982; Coatman et al. 2017; Runnoe et al. 2014; Zuo et al. 2020). These characteristics suggest that the CIV clouds are affected by nongravitational effects, such as outflows, which have a significant effect on the observed emission velocity profile. The so-called weak emission line quasar (WELQ, Diamond-Stanic et al. 2009, REW < 10 Å) population exhibits the largest blueshift (>3000 km s^{-1}, see e.g., Vietri et al. 2018). With a REW of ~150 Å, it is clear that PSO J191+86 does not belong to this QSO population, and therefore we do not expect to find a high value of blueshift for our source. Moreover, several works in the literature (e.g., Marziani et al. 1996; Sulentic et al. 2007; Richards et al. 2011) have claimed that RL sources usually show a lower value of blueshfit with respect to radio-quiet (RQ, or non-jetted) objects.

Other authors, have instead demonstrated that there is a consistency between the SE $M_{\rm BH}$ computed from CIV and Balmer lines (e.g., VP06; Greene et al. 2010; Assef et al. 2011;

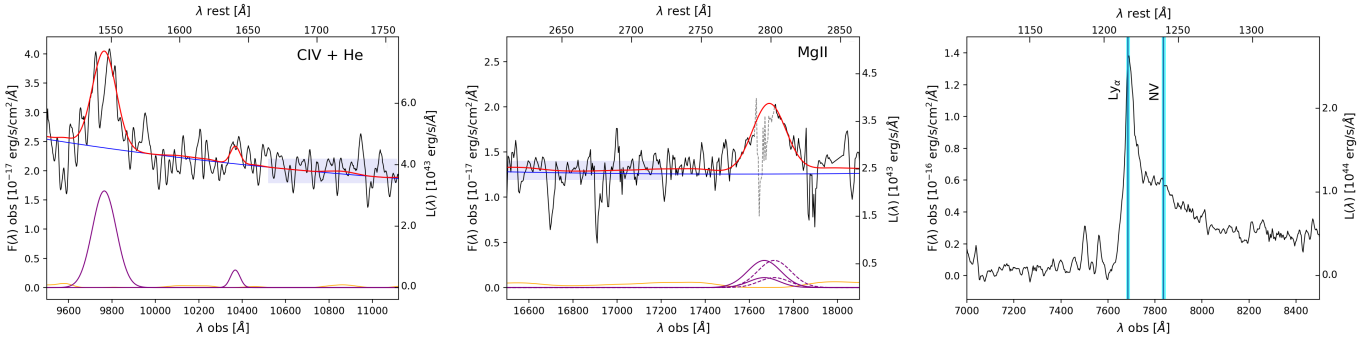

Fig. 6. Zoom into the CIV and MgII line fit and into the Ly$_\alpha$+NV region. *Left and central panel*: total spectral fit (red line), and the different components, i.e., power law + Balmer pseudo-continuum (blue line), Fe II template (orange line, from Vestergaard & Wilkes 2001), and emission lines (purple). For the MgII, we represent the two lines of the doublet (solid Gaussians and dashed Gaussians, respectively). Spectral regions used for the continuum fits are shown as horizontal light blue shaded areas. In the right panel, the absorption feature in the middle of the MgII line is masked (gray dotted line). *Right panel*: Ly$_\alpha$ and NV spectral region. The blue vertical lines represent the positions of the two BELs based on the MgII line redshift. The cyan shaded region is the uncertainty on this redshift estimate. The top x-axis reports the rest-frame wavelengths while the right axis shows the monochromatic luminosity.

Table 5. Properties of CIV and MgII BELs.

Emission line	Redshift	FWHM (km s^{-1})	REW (Å)	$F_{\rm line}$ (10^{-15} erg s^{-1} cm^{-2})	$L_{\rm line}$ (10^{44} erg s^{-1})	$M_{\rm BH}$ (10^9 $M_\odot$)
(1)	(2)	(3)	(4)	(5)	(6)	(7)
CIV	5.304±0.011	3762^{+124}_{-166}	$149.75^{+5.26}_{-4.82}$	$2.26^{+0.11}_{-0.08}$	$6.49^{+0.26}_{-0.17}$	$2.40^{+0.42}_{-0.39}$
MgII	5.320±0.005	2968^{+339}_{-395}	$66.15^{+16.11}_{-13.12}$	$0.61^{+0.17}_{-0.19}$	$1.85^{+0.54}_{-0.56}$	$1.67^{+0.40}_{-0.46}$

Notes. Column (1): emission line; Col. (2): redshift, estimated from the line peak; for the MgII we report the parameters of the single doublet line. The redshift of PSO J191+86 used throughout the paper is taken from the fit to the MgII BEL; Col. (3): FWHM in km s^{-1}; Col. (4): rest-frame equivalent width; Cols. (5) and (6): line flux and line luminosity; Col. (7): SE black hole mass. Here we report the statistical uncertainty computed by propagating the error on the FWHM and continuum luminosity. In the total mass error, the scaling relation scatter (0.55 dex for MgII and 0.36 dex for CIV) should be added.

Dalla Bontà et al. 2020). Finally, Shen et al. (2019) report that CIV can still be used because on average it provides black hole masses that are with those obtained from low-ionization lines, albeit with a large intrinsic scatter. Therefore, we decided to compute the black hole mass using the CIV, even if we considered our best estimate of mass to be those based on MgII.

For the MgII, we used the SE scaling relation presented by Vestergaard & Osmer (2009), for a direct comparison with other estimates in the literature:

$$M_{\rm BH} = 10^{6.86} \left[\frac{\rm FWHM\ (MgII)}{1000\,{\rm km\,s^{-1}}}\right]^2 \left[\frac{\lambda L_\lambda\ (3000\,{\rm Å})}{10^{44}\,{\rm erg\,s^{-1}}}\right]^{0.5}, \quad (1)$$

where $\lambda L_\lambda(3000\,{\rm Å})$ is the monochromatic luminosity at 3000 Å derived from the power-law model[3]: λL_λ (3000 Å) = 6.57±0.62×10^{46} erg s^{-1}. We obtained a black hole mass of $1.67^{+4.18}_{-1.26} \times 10^9\,M_\odot$. With respect to the uncertainty reported in Table 5, here the error on $M_{\rm BH}$ already takes into account the intrinsic scatter of the scaling relation (0.55 dex), which is the dominant uncertainty of the black hole mass estimate. Consistent black hole mass estimates are obtained using different scaling relations reported in the literature, both based on the continuum luminosity (e.g., McLure & Dunlop 2004; Shen & Liu 2012) and on the MgII line luminosity (e.g., Shen & Liu 2012).

[3] As the LUCI2 spectrum does not cover the wavelengths up to 3000 Å, we used the continuum near the MgII line, between 2720 Å and 2750 Å, and extrapolated it to 3000 Å using the power-law index estimated from our data ($\alpha_\lambda = -1.51$).

For the CIV, we used the scaling relation of VP06, which is the most frequently used in the literature:

$$M_{\rm BH} = 10^{6.66} \left[\frac{\rm FWHM\ (CIV)}{1000\,{\rm km\,s^{-1}}}\right]^2 \left[\frac{\lambda L_\lambda\ (1350{\rm Å})}{10^{44}\,{\rm erg\,s^{-1}}}\right]^{0.53}. \quad (2)$$

We estimated the continuum luminosity (λL_λ) at 1350 Å directly from the TNG rest frame spectrum: 6.78±0.97×10^{46} erg s^{-1}. Before applying this scaling relation, we corrected the FWHM (CIV) value for blueshift effect by following the prescription of Coatman et al. (2017):

$$\rm FWHM\ (CIV)\_corr = \frac{FWHM\ (CIV)}{\alpha \times \frac{\Delta_v}{1000\,km\,s^{-1}} + \beta}, \quad (3)$$

where α = 0.41±0.02, β = 0.62±0.04 and ΔV is the line blueshift defined as

$$\Delta V({\rm km\,s^{-1}}) = c \times \frac{1549.48\,{\rm Å} - \lambda_{\rm half}}{1549.48\,{\rm Å}}, \quad (4)$$

where c is the speed of light, 1549.48 Å is the rest frame wavelength for the CIV, and $\lambda_{\rm half}$ is the line centroid[4]. We found a ΔV of 741^{+350}_{-424} km s^{-1}, which is small, as expected, and allowed us to infer that the virial black hole mass of PSO J191+86 based

[4] The line centroid is defined as the wavelength that bisects the line, splitting it in two equal parts. We used the definition of Dalla Bontà et al. (2020): $\lambda_{\rm half} = \frac{\int \lambda P(\lambda) {\rm d}\lambda}{\int P(\lambda) {\rm d}\lambda}$, where $P(\lambda)$ is the line profile.

on CIV line should not be strongly affected by blueshift effects. A similar value of ΔV is found using $\lambda_{\rm peak}$ (i.e., the peak of the CIV line obtained by the Gaussian model in Fig. 6) with respect to $\lambda_{\rm half}$: 759±522 km s^{-1}.

The corrected FWHM (C IV) is 4072^{+180}_{-134} km s^{-1} and therefore the $M_{\rm BH}$ is equal to $2.40^{+3.11}_{-1.40} \times 10^9\,M_\odot$. The reported error already takes into consideration the intrinsic scatter of the used scaling relation (0.36 dex; VP06). By taking into account only the statistical uncertainty (see Table 5), the black hole mass derived from CIV is consistent within 1σ with that estimated from the MgII line.

6.2. Bolometric luminosity and Eddington ratio

The value of $M_{\rm BH}$ allowed us to derived the Eddington ratio for the source, which quantifies the speed with which the black hole is accreting with respect to the Eddington limit: $\lambda_{\rm Edd} = \frac{L_{\rm bol}}{L_{\rm Edd}}$, where $L_{\rm Edd}$ is the Eddington luminosity, the maximum luminosity beyond which radiation pressure will overcome gravity[5], and $L_{\rm bol}$ is the bolometric luminosity, which is the total energy produced by the AGN per unit of time integrated over all wavelengths. To estimate $L_{\rm bol}$, we used the continuum luminosity at 3000 Å computed in the previous subsection and the following bolometric correction: $L_{\rm bol} = K \times L_{3000\,\text{Å}}$, where $K = 5.15 \pm 1.26$ (Shen et al. 2008). We obtain $L_{\rm bol} = 3.38{\pm}1.14{\times}10^{47}$ erg s^{-1}. The corresponding value of $\lambda_{\rm Edd}$ is: $=1.55^{+1.08\ (3.50)}_{0.95\ (-1.37)}$. The uncertainty in parenthesis takes into account both the statistical error on the virial mass and the intrinsic scatter of the SE relation.

The SE $M_{\rm BH}$ and $\lambda_{\rm Edd}$ of PSO J191+86 are similar to those derived for RL and RQ QSOs discovered in the same range of redshift ($z = 4.5{-}5.5$; e.g., Shen et al. 2011; Yi et al. 2014; Trakhtenbrot et al. 2021; Diana et al. 2022). This similarity in terms of mass and Eddington ratio could be a consequence of a selection bias, as all these high-z sources have been selected from similar optical/IR surveys.

7. Analysis of the radio and X-ray properties

7.1. Radio spectrum

From the radio flux densities listed in Table 4, we computed the radio spectral index of PSO J191+86. We find that the radio spectrum shows a peak around ∼1 GHz (observed frame, Fig. 7, ∼6.3 GHz in the rest frame of the source). By assuming that the 1.4 GHz detection glimpses the turnover, we estimated the radio spectral indices below and above this potential peak and assuming a single power-law for the continuum emission ($S_\nu \propto \nu^{-\alpha}$). The spectral index between 325 MHz and 1.4 GHz ($\alpha^{1.4}_{0.325}$) is −0.93±0.28 and $\alpha^{4.85}_{1.4}$ (the spectral index between 1.4 and 4.85 GHz) is 0.65±0.12. Therefore, PSO J191+86 can be classified as a GPS source according to Healey et al. (2009).

As the radio data in hand are not simultaneous (spanning over ∼25 years), variability may be affecting the observed spectrum, making it appear flat (e.g., Dallacasa et al. 2000; Orienti & Dallacasa 2020). To date, we have no information about possible flux density variability of the source. A nearly simultaneous sampling of the radio spectrum (in particular below the possible turnover) is necessary.

[5] $L_{\rm Edd} = 1.26 \frac{M_{\rm BH}}{M_\odot} \times 10^{38}$ erg s^{-1}.

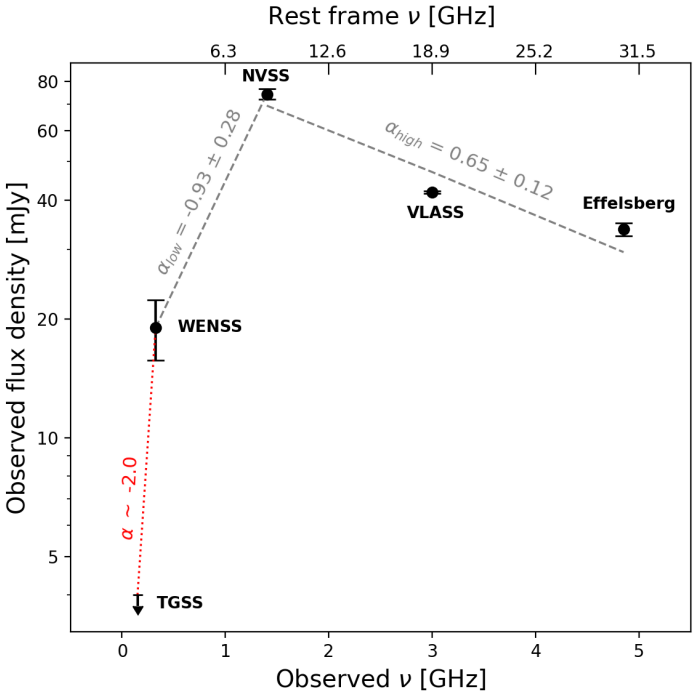

Fig. 7. Radio flux densities as a function of the observed (bottom x-axis) and rest-frame (top x-axis) frequency of PSO J191+86 from 0.150 to 4.85 GHz. The spectrum shows a peak around ∼1 GHz, and therefore the source can be classified as a GPS. The corresponding indices of the low- and high-frequency parts of the spectrum are reported together with the reference surveys. The red dashed line represents the possible spectral index according to the TGSS upper limit.

7.2. Radio loudness

From the observed radio and optical flux densities we computed the radio loudness (R) of PSO J191+86, which quantifies the level of power of the nonthermal synchrotron radio emission with respect to that of the thermal emission originating from the accretion disk. It is defined as the ratio between the rest-frame radio (5 GHz) and optical (blue band B at 4400 Å) fluxes (Kellermann et al. 1989): $R = \frac{S_{\rm 5\,GHz}}{S_{\rm 4400\,Å}}$. We estimated the flux density at 5 GHz by extrapolating the 1.4 GHz value adopting the spectral index of the optically thick part of the spectrum ($\alpha^{1.4}_{0.325}$). We highlight that 5 GHz in the rest-frame corresponds to 0.789 GHz in the observed frame. The value of the flux density at 4400 Å rest frame was derived from the LUCI2 rest-frame spectrum and assuming the optical spectral index of Vanden Berk et al. (2001, $\alpha_\nu = 0.44$). We obtained $R = 337 \pm 10$ (Log(R) = 2.52). This value is in agreement with that of other peaked radio sources at $z \geq 4.5$, but also with the R of the high-z blazars (e.g., Belladitta et al. 2019), i.e., RL AGN with the relativistic jets closely oriented to our line of sight (e.g., Urry & Padovani 1995). This may suggest that the nonthermal synchrotron emission of PSO J191+86 is Doppler boosted. Figure 8 shows the comparison between the radio luminosity at 8 GHz and the optical luminosity at 4400 Å of PSO J191+86 and of all the RL QSOs discovered in the literature at similar redshift ($z = 4.5{-}5.5$). For these RL QSOs, the luminosity at 8 GHz was computed starting from the observed flux at 1.4 GHz, and by assuming a radio spectral index of 0.75±0.25, as already done in other works (e.g., Bañados et al. 2015), as only a few sources have a tabulated spectral index in the literature. However, the observed 1.4 GHz frequency corresponds to

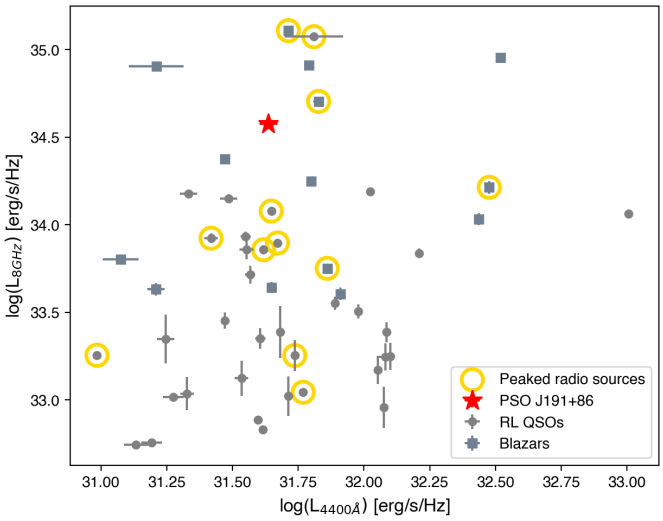

Fig. 8. Rest-frame radio luminosity at 8 GHz vs. the rest-frame optical luminosity at 4400 Å for PSO J191+86 (red star) compared with $z = 4.5–5.5$ radio-loud QSOs (gray points) discovered in the literature. Squares represent all the sources defined as blazars in the literature on the basis of their radio and/or X-ray properties. Yellow circles represent all the sources identified as peaked spectrum objects in the literature (Coppejans et al. 2017; Shao et al. 2020, 2022). PSO J191+86 is one of the most luminous RL QSOs at these redshifts, confirming the power of its radio emission.

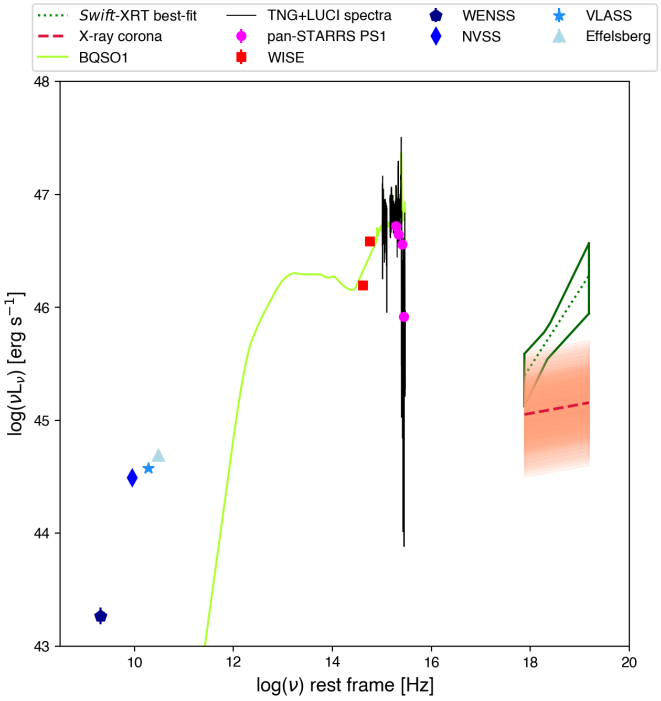

Fig. 9. Rest-frame SED of PSO J191+86 from radio to X-ray frequencies. In the X-ray, we show the best-fit emission in the observed [0.5–10] keV energy band (green dotted line) with its uncertainty. We also report the TNG and LUCI spectra (in black) and a quasar template (SWIRE template library; light-green) as a guide line. The red dashed line represents the coronal emission expected from a RQ AGN with the same $L_{2500\,Å}$ as PSO J191+86 according to the relation of Just et al. (2007), and the orange shaded area is the 1σ uncertainty on this estimate.

a rest-frame frequency of 7.7–9 GHz for $z = 4.5–5.5$ sources, which is very close to 8 GHz. Therefore, the lack of a measured spectral index has only a marginal impact on the computed radio luminosities. Instead the luminosity at 4400 Å was computed from the de-reddened z_{PS1} band magnitude (the one available for all these sources) and assuming the optical spectral index of Vanden Berk et al. (2001, $\alpha_\nu = 0.44$). From Fig. 8, it is clear that PSO J191+86 is one of the most luminous RL QSOs at this redshift, confirming that the radio emission is produced in a powerful jet. Further investigation is necessary to properly interpret the radio emission from PSO J191+86.

7.3. X-ray emission

From the X-ray properties reported in Sect. 5, we computed an X-ray luminosity of $5.33^{+1.54}_{-1.31}\times10^{45}$ erg s^{-1} in the [2–10] keV energy band[6]. This value clearly tells us that the X-ray emission of PSO J191+86 largely overwhelms that expected from a typical hot X-ray corona and therefore originates in a powerful jet. This is particular evident when plotting the SED of PSO J191+86 (Fig. 9): the X-ray emission is flatter and stronger with respect to that of RQ AGN with the same optical luminosity, according to the L_X–L_{UV} relation of Just et al. (2007).

The value of the photon index (Γ_X) computed from the *Swift*-XRT observation (Sect. 5) is flat (<1.5), in line with that of peaked radio sources (e.g., Snios et al. 2020) and blazars (e.g., Ighina et al. 2019) at high redshift. Therefore, we cannot exclude that the X-ray emission of PSO J191+86 is dominated by a relativistic jet oriented toward the Earth, as the high value of R suggests as well. This is also indicated by the value of the $\tilde{\alpha}_{ox}$ of PSO J191+86, the ratio that quantifies the relative strength of the X-ray emission with respect to the optical/UV component. The $\tilde{\alpha}_{ox}$ is the two-point spectral index of a fictitious power law connecting 2500 Å and 10 keV in the rest frame of the source (Ighina et al. 2019): $\tilde{\alpha}_{ox} = -0.3026 \times \log(\frac{L_{10\,keV}}{L_{2500\,Å}})$. The value of the monochromatic luminosity at 10 keV rest frame was computed from the observed flux density at [0.5–10] keV and using the α_X value[7]: $L_{10\,keV} = 2.25^{+0.45}_{-0.41}\times10^{27}$ erg s^{-1} Hz^{-1}. The luminosity at 2500 Å was instead measured from the flux density at 2500 Å directly obtained from the LUCI 2 rest-frame spectrum: $L_{2500\,Å} = 5.56\pm0.40\times10^{31}$ erg s^{-1} Hz^{-1}. We found an $\tilde{\alpha_{ox}}$ equal to $1.329^{+0.027}_{-0.025}$, which is similar to that of high-z blazars (e.g., Ighina et al. 2019).

8. Discussion and conclusions

In this work, we present the discovery and multi-wavelength properties of PSO J191+86, a powerful radio QSO in the early Universe ($z = 5.32$). In the radio band, PSO J191+86 shows a possible peaked radio spectrum around ~1 GHz in the observed frame, corresponding to ~6.3 GHz in the rest frame. If this turnover is confirmed, PSO J191+86 will be one of the most powerful ($L_{1.4\,GHz} = 1.17\times10^{28}$ W Hz^{-1}) GPS source at $z > 5$ ever discovered.

Assuming that the radio spectrum is peaked, we can compute the kinetic age of PSO J191+86 radio jets from the well-known correlation between peak frequency (ν_t in GHz) and projected

[6] $L_{02-10\,keV} = 4\pi D_L^2 (1+z)^{\alpha_X-1} F[2-10\,keV]$, where z is the redshift estimated from the MgII line (see Table 5) and D_L is the corresponding luminosity distance computed on https://www.astro.ucla.edu/~wright//CosmoCalc.html.

[7] $L_{10\,keV} = \frac{L_{0.5-10\,keV}\nu_{10\,keV}(-\alpha_X+1)}{(\nu_{10\,keV}^{-\alpha_X+1} - \nu_{0.5\,keV}^{-\alpha_X+1})}$.

angular size (l in kpc) derived by O'Dea & Baum (1997):

$$log(\nu_t) = -0.21(\pm0.05) - 0.65(\pm0.05)\log(l). \quad (5)$$

Assuming that the peak of the spectrum is between 1 and 2 GHz (observed frame, i.e., ∼6 and ∼13 GHz in the rest-frame), we obtain l in the range ∼10–30 pc (without taking into account the large scatter of the ν_t–l relation; e.g., Nyland et al. 2020). The corresponding kinetic age of the radio jets of PSO J191+86 would be in the range of ∼150–460 yr, assuming a typical hot spot expansion velocity of 0.2c (e.g., Giroletti & Polatidis 2009; An & Baan 2012). This would make PSO J191+86 one of the youngest GPS source at $z \sim 5$ ever discovered. Therefore, a detailed study of its radio emission could shed light on the triggering of radio activity in this distant QSO, on the formation and early stage evolution of its radio jets, on their interaction with the ambient medium, and on their feedback on the host galaxy (e.g., Hardcastle & Croston 2020). However, the nonsimultaneity of the radio data at hand prevents us from assessing the real nature of the radio spectrum because of possible variability. Simultaneous observations over a wide range of frequencies are necessary to confirm the possible turnover.

The radio loudness of the source is very high (>300), making PSO J191+86 similar to the bulk population of blazars in the early Universe. Moreover, the flat ($\Gamma_X = 1.32$) and strong X-ray emission with respect to the optical emission ($\tilde{\alpha_{ox}} = 1.329$) is similar to that of blazars. Therefore, PSO J191+86 could be a GPS object with the young relativistic jets oriented toward our line of sight. This is not uncommon at high-z, because the blazar Q0906+6930 (Romani et al. 2004) at $z = 5.47$ shows a clearly peaked radio spectrum (e.g., Coppejans et al. 2017; Mufakharov et al. 2021) with a turnover frequency of 6.4 GHz (observed frame), but, at the same time, Very Long Baseline Interferometry (VLBI) data found evidence of Doppler boosting (e.g., An et al. 2020). These results suggest that J0906+6930 is a GPS source likely oriented toward the observer. Similarly a multifrequency VLBI follow up for PSO J191+86 is in progress (Belladitta et al., in prep.) that is designed to spatially resolve the parsec-scale radio emission of the source and to find evidence of Doppler boosting.

Acknowledgements. We thank the anonymous referee for the useful comments and suggestions. This work is based on observations made with the Large Binocular Telescope (LBT, program LBT2018AC123500-1). We are grateful to the LBT staff for providing the observations for this object. LBT is an international collaboration among institutions in the United States of America, Italy, and Germany. This work is based on observations made with the Italian Telescopio Nazionale *Galileo* (TNG) operated on the island of La Palma by the Fundación Galileo Galilei of the INAF (Istituto Nazionale di Astrofisica) at the Spanish Observatorio del Roque de los Muchachos of the Instituto de Astrofisica de Canarias. The observations were executed by M. Pedani on a night with a short slot of DDT time available. This work also used data from observations with the Neil Gehrels Swift Observatory (program ID: 3110833). This work made use of data supplied by the UK Swift Science Data Centre at the University of Leicester. SB, AC and AM acknowledge financial contribution from the agreement ASI-INAF n. I/037/12/0 and n.2017-14-H.0 and from INAF under PRIN SKA/CTA FORECaST. CS acknowledges financial support from the Italian Ministry of University and Research – Project Proposal CIR01_00010. This project used public archival data from the first data release of the Panoramic Survey Telescope and Rapid Response System (Pan-STARRS PS1) . Pan-STARRS1 PS1 have been made possible through contributions of the institutes listed in https://panstarrs.stsci.edu. The NVSS data was taken by the NRAO Very Large Array. The National Radio Astronomy Observatory is a facility of the National Science Foundation operated under cooperative agreement by Associated Universities, Inc. GMRT is run by the National Centre for Radio Astrophysics of the Tata Institute of Fundamental Research. WENSS is a joint project of the Netherlands Foundation for Research in Astronomy (NFRA) and Leiden Observatory. VLASS data have been obtained from the Canadian Astronomy Data Centre operated by the National Research Council of Canada with the support of the Canadian Space Agency. The Canadian Initiative for Radio Astronomy Data Analysis (CIRADA) is funded by a grant from the Canada Foundation for Innovation 2017 Innovation Fund (Project 35999) and by the Provinces of Ontario, British Columbia, Alberta, Manitoba and Quebec, in collaboration with the National Research Council of Canada, the US National Radio Astronomy Observatory and Australia's Commonwealth Scientific and Industrial Research Organisation. This research made use of Astropy, a community-developed core Python package for Astronomy (Astropy Collaboration 2018).

References

An, T., & Baan, W. A. 2012, ApJ, 760, 77
An, T., Mohan, P., Zhang, Y., et al. 2020, Nat. Commun., 11, 143
Assef, R. J., Denney, K. D., Kochanek, C. S., et al. 2011, ApJ, 742, 93
Astropy Collaboration (Price-Whelan, A. M., et al.) 2018, AJ, 156, 123
Bañados, E., Venemans, B. P., Morganson, E., et al. 2015, ApJ, 804, 118
Bañados, E., Carilli, C., Walter, F., et al. 2018, ApJ, 861, L14
Bañados, E., Mazzucchelli, C., Momjian, E., et al. 2021, ApJ, 909, 80
Belladitta, S., Moretti, A., Caccianiga, A., et al. 2019, A&A, 629, A68
Belladitta, S., Moretti, A., Caccianiga, A., et al. 2020, A&A, 635, L7
Bisogni, S., di Serego Alighieri, S., Goldoni, P., et al. 2017, A&A, 603, A1
Blandford, R., Meier, D., & Readhead, A. 2019, ARA&A, 57, 467
Caccianiga, A., Moretti, A., Belladitta, S., et al. 2019, MNRAS, 484, 204
Carnall, A. C., Shanks, T., Chehade, B., et al. 2015, MNRAS, 451, L16
Chambers, K. C., Magnier, E. A., Metcalfe, N., et al. 2016, ArXiv e-prints [arXiv:1612.05560]
Coatman, L., Hewett, P. C., Banerji, M., et al. 2017, MNRAS, 465, 2120
Condon, J. J., Cotton, W. D., Greisen, E. W., et al. 1998, AJ, 115, 1693
Coppejans, R., van Velzen, S., Intema, H. T., et al. 2017, MNRAS, 467, 2039
Corbin, M. R., & Boroson, T. A. 1996, ApJS, 107, 69
Cutri, R. M., Wright, E. L., Conrow, T., et al. 2012, Explanatory Supplement to the WISE All-Sky Data Release Products
Dalla Bontà, E., Peterson, B. M., Bentz, M. C., et al. 2020, ApJ, 903, 112
Dallacasa, D., Stanghellini, C., Centonza, M., & Fanti, R. 2000, A&A, 363, 887
De Rosa, G., Venemans, B. P., Decarli, R., et al. 2014, ApJ, 790, 145
Diamond-Stanic, A. M., Fan, X., Brandt, W. N., et al. 2009, ApJ, 699, 782
Diana, A., Caccianiga, A., Ighina, L., et al. 2022, MNRAS, 511, 5436
Evans, P. A., Beardmore, A. P., Page, K. L., et al. 2009, MNRAS, 397, 1177
Fabian, A. C. 2012, ARA&A, 50, 455
Farina, E. P., Schindler, J. T., Walter, F., et al. 2022, ApJ, 941, 106
Fitzpatrick, E. L. 1999, PASP, 111, 63
Gargiulo, A., Fumana, M., Bisogni, S., et al. 2022, MNRAS, 514, 2902
Gaskell, C. M. 1982, ApJ, 263, 79
Giroletti, M., & Polatidis, A. 2009, Astron. Nachr., 330, 193
Greene, J. E., Peng, C. Y., & Ludwig, R. R. 2010, ApJ, 709, 937
Hardcastle, M. J., & Croston, J. H. 2020, New Astron. Rev., 88, 101539
Healey, S. E., Fuhrmann, L., Taylor, G. B., Romani, R. W., & Readhead, A. C. S. 2009, AJ, 138, 1032
Ighina, L., Caccianiga, A., Moretti, A., et al. 2019, MNRAS, 489, 2732
Ighina, L., Caccianiga, A., Moretti, A., et al. 2023, MNRAS, 519, 2060
Intema, H. T., Jagannathan, P., Mooley, K. P., & Frail, D. A. 2017, A&A, 598, A78
Just, D. W., Brandt, W. N., Shemmer, O., et al. 2007, ApJ, 665, 1004
Kalberla, P. M. W., Burton, W. B., Hartmann, D., et al. 2005, A&A, 440, 775
Karouzos, M., Woo, J.-H., Matsuoka, K., et al. 2015, ApJ, 815, 128
Kellermann, K. I., Sramek, R., Schmidt, M., Shaffer, D. B., & Green, R. 1989, AJ, 98, 1195
Lacy, M., Baum, S. A., Chandler, C. J., et al. 2020, PASP, 132
Liu, Y., Wang, R., Momjian, E., et al. 2021, ApJ, 908, 124
Mainzer, A., Bauer, J., Grav, T., et al. 2011, ApJ, 731, 53
Marziani, P., Sulentic, J. W., Dultzin-Hacyan, D., Calvani, M., & Moles, M. 1996, ApJS, 104, 37
Marziani, P., Sulentic, J. W., Negrete, C. A., et al. 2010, MNRAS, 409, 1033
Marziani, P., Sulentic, J. W., Plauchu-Frayn, I., & del Olmo, A. 2013, A&A, 555, A89
Marziani, P., del Olmo, A., Martínez-Carballo, M. A., et al. 2019, A&A, 627, A88
Massaro, F., Giroletti, M., D'Abrusco, R., et al. 2014, ApJS, 213, 3
Mazzucchelli, C., Bañados, E., Venemans, B. P., et al. 2017, ApJ, 849, 91
McGreer, I. D., Becker, R. H., Helfand, D. J., & White, R. L. 2006, ApJ, 652, 157
McLure, R. J., & Dunlop, J. S. 2004, MNRAS, 352, 1390
McMullin, J. P., Waters, B., Schiebel, D., Young, W., & Golap, K. 2007, ASP Conf. Ser., 376, 127
Mufakharov, T., Mikhailov, A., Sotnikova, Y., et al. 2021, MNRAS, 503, 4662
Nyland, K., Dong, D. Z., Patil, P., et al. 2020, ApJ, 905, 74
O'Dea, C. P., & Baum, S. A. 1997, AJ, 113, 148

O'Dea, C. P., & Saikia, D. J. 2021, A&ARv, 29, 3
Oke, J. B. 1990, AJ, 99, 1621
Orienti, M., & Dallacasa, D. 2020, MNRAS, 499, 1340
Padovani, P., Alexander, D. M., Assef, R. J., et al. 2017, A&ARv, 25, 2
Raiteri, C. M., Acosta Pulido, J. A., Villata, M., et al. 2020, MNRAS, 493, 2793
Rakshit, S., Stalin, C. S., & Kotilainen, J. 2020, ApJS, 249, 17
Rengelink, R. B., Tang, Y., de Bruyn, A. G., et al. 1997, A&AS, 124, 259
Romani, R. W., Sowards-Emmerd, D., Greenhill, L., & Michelson, P. 2004, ApJ, 610, L9
Richards, G. T., Kruczek, N. E., Gallagher, S. C., et al. 2011, AJ, 141, 167
Runnoe, J. C., Brotherton, M. S., DiPompeo, M. A., & Shang, Z. 2014, MNRAS, 438, 3263
Sbarrato, T., Ghisellini, G., Nardini, M., et al. 2012, MNRAS, 426, L91
Schindler, J.-T., Farina, E. P., Bañados, E., et al. 2020, ApJ, 905, 51
Seifert, W., Appenzeller, I., Baumeister, H., et al. 2003, SPIE Conf. Ser., 4841, 962
Shao, Y., Wagg, J., Wang, R., et al. 2020, A&A, 641, A85
Shao, Y., Wagg, J., Wang, R., et al. 2022, A&A, 659, A159
Shen, Y., & Liu, X. 2012, ApJ, 753, 125
Shen, Y., Greene, J. E., Strauss, M. A., Richards, G. T., & Schneider, D. P. 2008, ApJ, 680, 169
Shen, Y., Richards, G. T., Strauss, M. A., et al. 2011, ApJS, 194, 45
Shen, Y., Wu, J., Jiang, L., et al. 2019, ApJ, 873, 35
Snios, B., Siemiginowska, A., Sobolewska, M., et al. 2020, ApJ, 899, 127
Sulentic, J. W., Bachev, R., Marziani, P., Negrete, C. A., & Dultzin, D. 2007, ApJ, 666, 757
Tang, B., Shang, Z., Gu, Q., Brotherton, M. S., & Runnoe, J. C. 2012, ApJS, 201, 38
Tody, D. 1993, ASP Conf. Ser., 52, 173
Trakhtenbrot, B. 2021, IAU Proc. 356, 261
Trakhtenbrot, B., & Netzer, H. 2012, MNRAS, 427, 3081
Urry, C. M., & Padovani, P. 1995, PASP, 107, 803
Vanden Berk, D. E., Richards, G. T., Bauer, A., et al. 2001, AJ, 122, 549
Vestergaard, M. 2002, ApJ, 571, 733
Vestergaard, M., & Osmer, P. S. 2009, ApJ, 699, 800
Vestergaard, M., & Peterson, B. M. 2006, ApJ, 641, 689
Vestergaard, M., & Wilkes, B. J. 2001, ApJS, 134, 1
Vietri, G., Piconcelli, E., Bischetti, M., et al. 2018, A&A, 617, A81
Vito, F., Mignoli, M., Gilli, R., et al. 2022, A&A, 663, A159
Volonteri, M., Silk, J., & Dubus, G. 2015, ApJ, 804, 148
Wills, B. J., Brotherton, M. S., Fang, D., Steidel, C. C., & Sargent, W. L. W. 1993, ApJ, 415, 563
Wright, E. L., Eisenhardt, P. R. M., Mainzer, A. K., et al. 2010, AJ, 140, 1868
Yi, W.-M., Wang, F., Wu, X.-B., et al. 2014, ApJ, 795, L29
Zeimann, G. R., White, R. L., Becker, R. H., et al. 2011, ApJ, 736, 57
Zuo, W., Wu, X.-B., Fan, X., et al. 2020, ApJ, 896, 40